Spin Crossover Induced by Changing the Identity of the Secondary Metal Ion from Pd^{II} to Ni^{II} in a Face-Centered $Fe^{II}_8M^{II}_6$ Cubic Cage

*Hyunsung Min, Alexander R. Craze†, Matthew J. Wallis, Ryuya Tokunaga, Takahiro Taira, Yutaka Hirai, Mohan M. Bhadbhade, Daniel J. Fanna, Christopher E. Marjo, Shinya Hayami, Leonard F. Lindoy and Feng Li**

Keywords: Spin crossover, cubic cage, heterometallic

ABSTRACT

The engineering of spin crossover (SCO) coordination cages is a complex endeavor with great potential in next generation multifunctional materials. Discrete metallosupramolecular cages exhibiting SCO are an exciting, though rare, class of porous polyhedral material. Incorporating the SCO property into these architectures is complicated, as there are many inter- and intramolecular factors which must be appropriately balanced. Previous investigations into the magnetic properties of a large cubic metallosupramolecular cage, $[Fe_8Pd_6\mathbf{L}_8]^{28+}$, constructed using semi-rigid metalloligands, found that the Fe(II) centers that occupied the corners of the cubic structure did not undergo a spin transition. In this work, substitution of the linker metal on the face of the cage resulted in spin crossover behavior, as evidenced by magnetic susceptibility, Mössbauer and single crystal X-ray diffraction. Structural comparisons of these two cages were undertaken to shed light on the possible mechanism responsible for switching of the $[Fe_8M^{II}_6\mathbf{L}_8]^{28+}$ architecture from SCO inactive to active by simply changing the identity of M(II). This led to the suggestion that a possible interplay of intra- and intermolecular interactions may permit SCO in the Ni(II) analogue, **1**. The distorted octahedral coordination environment of the secondary Ni(II) centers occupying the cage faces provided conformational flexibility for the eight metalloligands of the cubic architecture relative to the square planar Pd(II) environment. Meanwhile the occupation of axial coordination sites of the Ni(II) cations by CH_3CN prevented the close packing of cages observed for the Pd(II) analogue, leading to a more offset, distant packing arrangement of cages in the lattice, whereby important areas of the cage that were shown to change most dramatically with SCO experienced a lesser degree of steric hindrance. Design via the effect of secondary metal centers on the flexibility of metalloligand structures and the effect of the axial donors on the packing arrangements may serve as new routes for engineering cage systems with desired magnetic properties.

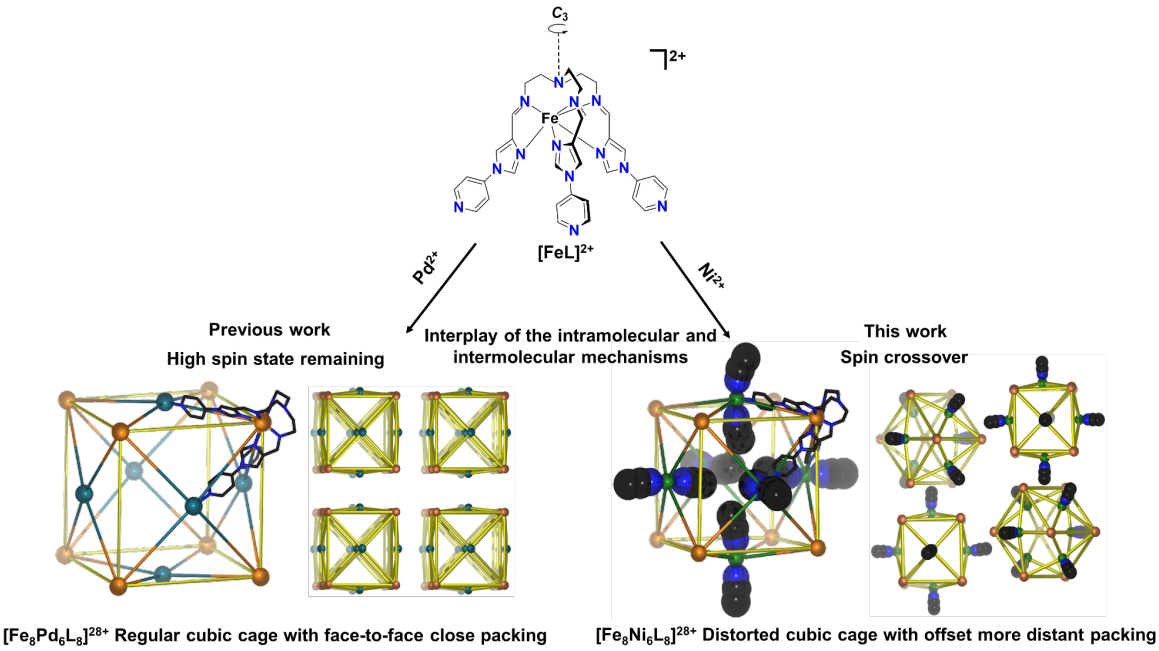
C3
2+
Fe
[FeL]2+
Pd2+
Ni2+
Previous work
High spin state remaining
Interplay of the intramolecular and intermolecular mechanisms
This work
Spin crossover
[Fe8Pd6L8]28+ Regular cubic cage with face-to-face close packing
[Fe8Ni6L8]28+ Distorted cubic cage with offset more distant packing

INTRODUCTION

The design and assembly of discrete polynuclear materials that incorporate an internal cavity remains an active goal in metallosupramolecular chemistry.[1,2] Such molecules have shown potential in a range of applications which take advantage of host-guest interactions, including sensing,[3-6] catalysis,[7-10] drug encapsulation[11,12] and the selective uptake of guest molecules[13-16]. In addition, there has been continuing interest in the construction of new cage systems as photoactive[17-19] and magnetic materials,[20] with the latter including spin crossover (SCO) systems.[21-42] Currently, there exists a large structural diversity of metallo-organic cages, owing to the development of multiple synthetic strategies that frequently involve metal-directed self-assembly.[1,2,43-45] One widely employed strategy is the metalloligand approach.[23,46-54] Variation of the nature of the metal ions and ligand scaffold can direct cage assembly, and has resulted in the construction of a variety of cage topologies, motivated by the search for increased functionality and complexity.[55] In particular, interest in heterometallic cage systems has increased greatly over recent years as a result of their potential for multifunctionality.[20]

SCO behavior has widely been reported for homometallic cages,[21-22,24-27,34-37,41] with reports of heterometallic SCO systems being less common.[23,38-40] The majority of SCO systems reported for coordination cages demonstrate gradual and incomplete spin transitions,[21-27,34-42] with only a few demonstrating complete ST.[22,36] Upon SCO, the coordination environment of the active metal center must be able to undergo a significant conformational change. In large polynuclear cages, take cubic cages for instance, for complete SCO to occur, eight metal centers must undergo SCO. As such, these architectures must have the capacity for such substantial conformational changes to occur in the coordination environment of all eight SCO sites. This could place a severe intramolecular steric strain on the cage architecture, and unless the required conformational

changes are cooperative, these strains may inhibit the ability of some metal centers to undergo SCO. For those cages that do exhibit a complete (or near complete) SCO, the ligand scaffold will normally incorporate flexible linkers, thus providing the necessary conformational freedom to compensate for the changes in the metal coordination environments.[36,41] Conversely, in the case of cages constructed from rigid ligand building blocks, complete SCO is less frequently observed.[23,38,42] A popular design for heterometallic coordination cages associated with SCO properties has involved a cubic architecture that possesses eight metal ions (often Fe(II)) at the corner of the cube while six secondary metal ions occupy the faces (see Figure 1).[23,38] Such an overall design allows for further control of the cage's architecture through variation of the binding modes (as well as the affinities) of the primary and secondary metal ions, along with the possibility of enhanced functionality arising through the use of heterometal ions (whose coordination environments are also open to be 'tuned').[23,34,38-40]

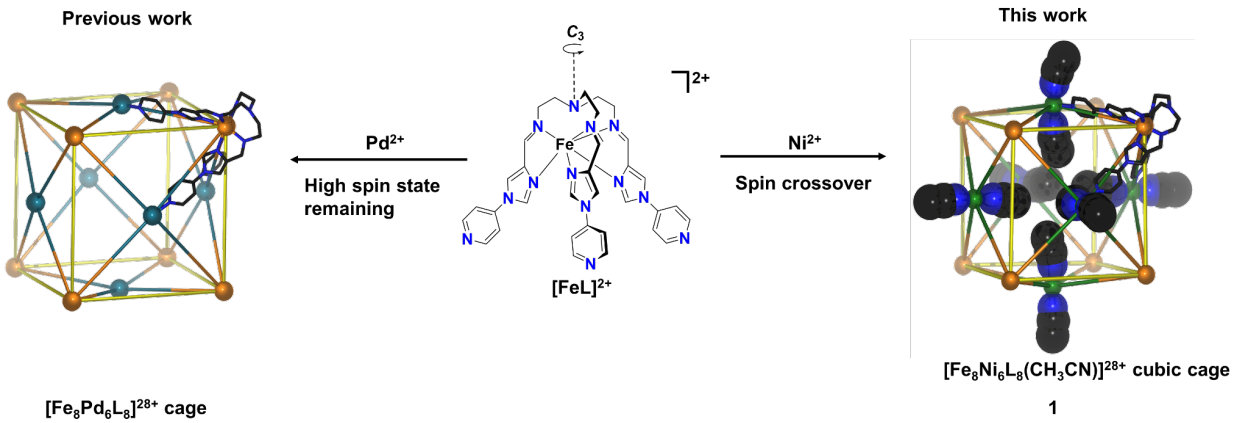

Figure 1. Schematic representation of the synthesis of a SCO inactive $[Fe_8Pd_6\mathbf{L}_8]^{28+}$ cage and its $[Fe_8Ni_6\mathbf{L}_8(CH_3CN)_{12}]^{28+}$ SCO active analogue, **1**, obtained using the metalloligand $[Fe\mathbf{L}]^{2+}$.

Recently, we reported a $[Fe_8Pd_6\mathbf{L}_8]^{28+}$ tetradecanuclear cubic cage,[47] obtained via use of the semi-rigid high spin (HS) tripodal metalloligand $[Fe\mathbf{L}]^{2+}$ in which eight Fe(II) ions are located at the corners of the cube while Pd(II) ions occupy each of the six faces (see Figure 1); close face-to-

face packing of individual cages is present in the solid state. No SCO was observed for this structure (which remained HS even at low temperatures). In this study, we report the synthesis of an analogous structure that differs in that the facial metal centers are now Ni(II) to form a $[Fe_8Ni_6\mathbf{L}_8(CH_3CN)_{12}]^{28+}$ heterometallic cubic cage, (**1**). On changing the square planar, four coordinate Pd(II) centers to distorted octahedral Ni(II) centers, SCO was observed by both crystallographic and magnetic measurements, with the SCO influenced by the degree of solvation present. This emergence of SCO behavior in the solid state may be influenced by three factors — the electronic structure of the secondary M(II) ion, the geometric flexibility of the secondary M(II) ion or the crystal packing arrangement of the cages.

Herein we report the synthesis of **1** using the metalloligand approach along with its characterization by magnetic, variable temperature single crystal X-ray diffraction (VT-SCXRD), CHN analysis, scanning electron microscopy-energy dispersive spectroscopy (SEM-EDS) and thermogravimetric analysis and differential scanning calorimetry (TGA-DSC). Furthermore, the magnetostructural correlations are explored to elucidate the possible mechanism by which the $[Fe_8M(II)_6\mathbf{L}_8]^{28+}$ architecture may switch from SCO inactive to SCO active on changing the identity of M(II) from Pd(II) to Ni(II).

Results and Discussion

*Synthesis and Characterisation of **1***

The HS Fe(II) metalloligand $[Fe\mathbf{L}]^{2+}$ was prepared by the reported method.[47] Self assembly of the heterobimetallic cage **1** was carried out by the addition of $Ni(BF_4)_2$ to a solution of $[Fe\mathbf{L}]^{2+}$ in acetonitrile in a 4:3 stoichiometric ratio. Slow vapor diffusion of di-isopropyl ether into the reaction mixture in acetonitrile (CH_3CN) yielded dark orange/red block crystals (Figure S1) which

were separated by filtration and air dried to give 57.0% yield of **1,** which has been fully characterized by CHN, SEM-EDS, VT-SCXRD and TGA-DSC analysis. The SEM images of **1** demonstrate the trapezoidal morphology of **1** and the decay that occurs upon losing solvent. Moreover EDS analysis confirmed the presence of C, N, F, Fe and Ni and the ratio of Fe(II) to Ni(II) in the cage to be approximately 4:3 (Figure S2). The element maps of **1** demonstrate that each element was uniformly distributed throughout the crystal, showing chemical homogeneity (Figure S2). A mass loss of -7.46 % was observed in TGA experiments (Figure S3), which also showed that **1** begins to decompose from 610.2 K (Figure S3). TGA-DSC measurements demonstrate the presence of similar amounts of water molecules in the CHN analyses that was conducted with bulk samples of **1**.

Single Crystal X-ray Diffraction

VT-SCXRD experiments were conducted on a dark orange/red block crystal at 100, 150, 200, 250 and 275 K. The X-ray structure confirmed the formation of a heteronuclear cubic cage **1** (Figure 2), which crystallized in the monoclinic space group $P2_1/c$ (Table S1). The asymmetric unit at 100 K consists of one complete cage, with five disordered tetrafluoroborate anions resolved, both within and outside the internal cage cavity. As the temperature of the measurements were increased, thermally induced disorder meant the number of tetrafluoroborate (BF_4^-) anions that were able to be resolved decreased, until at 250 K where no anions were resolved. Furthermore, **1** exhibits both possible homochiral enantiomers (*Δ* and *Λ*) with all [Fe**L**]$^{2+}$ metalloligand centers of the cage being in either the *Λ Λ Λ Λ Λ Λ Λ Λ* or *Δ Δ Δ Δ Δ Δ Δ Δ* configuration. Each secondary Ni(II) metal center coordinates equatorially with four distal pyridyl nitrogens of four different metalloligands to form a pseudo fourfold symmetry axes of the cubic cage, with two nitrogens

from CH_3CN in the axial positions to form a distorted octahedral coordination environment (Figure 2).

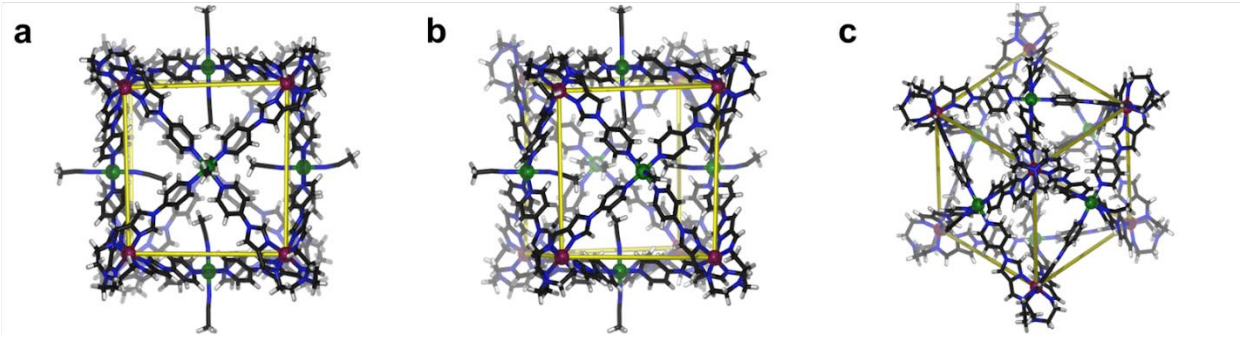

Figure 2. SCXRD structure of **1** at 100 K, shown a) down the pseudo C_4 axis, b) in an offset view and c) down the pseudo C_3 axis. The BF_4^- anions and solvent molecules are omitted for clarity (Fe, purple; Ni, green; C, black; N, blue; H, white).

The octahedral distortion parameters describing the average coordinate bond length and the angular parameters representing the sum of deviations of each octahedral *cis* bond from 90° (Σ) and the sum of deviations from 60° of the *cis* bonds as projected in a plane orthogonal to the pseudo threefold axes of the octahedron (Θ) were calculated using OctaDist[56] to gauge the spin state at each Fe(II) center (Table 1). The average Fe-$N_{imidazolimine}$ bond lengths (2.17 Å at 275 K and 1.97 Å at 100 K) and average octahedral distortion (Σ) values (105.0˚ at 275 K and 55.1˚ at 100 K) of **1** are in accord with HS and low spin (LS) values at 275 and 100 K respectively (Table 1). The plots of both the average Fe-$N_{imidazolimine}$ bond lengths and the Fe-$N_{imidazolimine}$ bond lengths of each of the eight Fe(II) centers of **1** as a function of temperature (Figure 3) show a sigmoidal behavior indicative of SCO in all Fe(II) centers. This is further corroborated by values of Θ at 100 and 275 K (181.1˚ and 273.0˚ respectively).

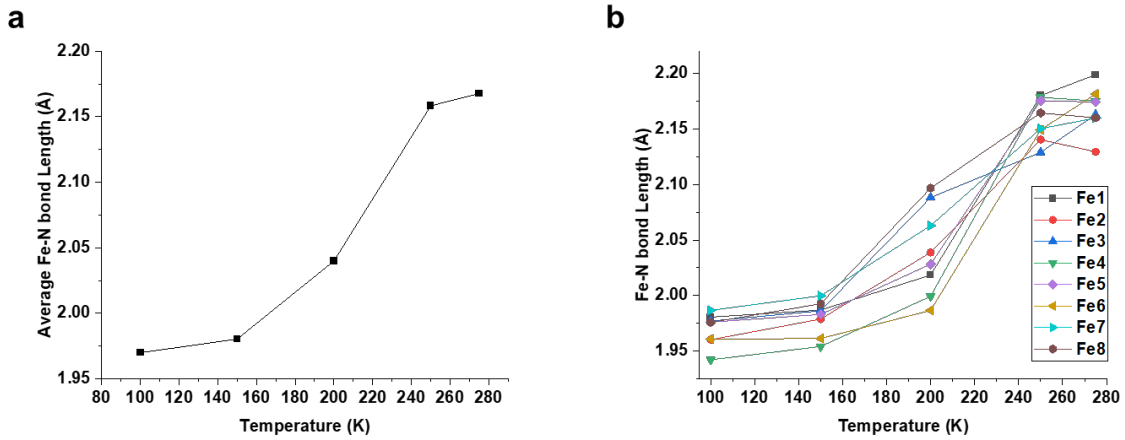

Figure 3. Plots of a) average Fe-N bond lengths and b) individual Fe-N bond lengths for each of the eight Fe(II) centers of **1** as a function of temperature.

Table 1. Various crystallographic parameters of the previously reported metalloligand $[Fe\mathbf{L}]^{2+}$ and $[Fe_8Pd_6\mathbf{L}_8]^{28+}$ cage,[47] as well as **1**, obtained through VT-SCXRD.

Compound	Average Fe-N Bond Length (Å)	Σ (°)	Θ (°)	Average Fe···Fe Distance (Å)[a]	Average M···M Distance (M = Ni, Pd) (Å)[b]	Crystal Packing Coefficient[c] (%)
$[Fe\mathbf{L}]^{2+}$ (100 K)	2.20	105.0	280.4	N/A	N/A	54.6
$[Fe_8Pd_6\mathbf{L}_8]^{28+}$ (100 K)	2.19	131.3	374.1	25.21	16.30	33.4
1 (100 K)	1.97	55.1	181.1	24.86	17.26	28.7
1 (150 K)	1.98	57.0	189.7	24.90	17.29	28.3
1 (200 K)	2.04	70.3	220.3	25.15	17.17	27.9

1 (250 K)	2.16	105.2	279.6	25.65	16.98	26.6
1 (275 K)	2.17	105.0	273.0	25.58	16.80	27.0

[a] Intramolecular Fe···Fe distance along a pseudo threefold symmetry axis. [b] Intramolecular M···M distance along the pseudo fourfold symmetry axis (M = Ni or Pd). [c] Calculated as the percentage volume of the unit cell occupied by the cage structure (for more detail see S3.3 in the ESI).

Magnetic Susceptibility

The magnetic susceptibility experiments were conducted on solvated and desolvated samples of **1**, with LIESST experiments being conducted on the solvated sample only. The solvated materials exhibited a gradual, two-step and incomplete spin transition (Figure 4a and S4) over the temperature range of 5-400 K. At 400 K a $\chi_m T$ of 34.64 cm^3 K mol^{-1} corresponds to all eight Fe(II) centers in the HS configuration, as well as six non-interacting paramagnetic Ni(II) centers.[57] The gradual decrease in susceptibility was observed to possess two $T_{1/2}$ values of 325 and 192 K (Figure S4). The susceptibility then plateaued at 50 K at 24.19 cm^3 K mol^{-1}, representative of three Fe(II) centers having transitioned to the LS state. The susceptibility was then observed to fall off sharply due to zero field splitting in residual paramagnetic Fe(II) and Ni(II) at low temperatures. To test for scan rate dependencies, the sample was then cycled at 1 and 4 K min^{-1}, and both were consistent (Section S4 of the ESI).

Next, to examine the effect of solvent loss, after successive heating and cooling cycles solvated **1** was held at 400 K for a 60 minute isotherm to induce loss of solvent. The magnetic susceptibility of desolvated **1** at 4 K min^{-1} demonstrated a similar gradual, two-step incomplete spin transition (Figure 4a and S4), with similar $\chi_m T$ values from 300 to 400 K, although with a consistently higher $\chi_m T$ value from 300 to 400 K compared to solvated **1** (Figure 4a). The $\chi_m T$ values of desolvated **1**

closely matched that of the solvated sample at 400 K, which from 34.59 cm^3 K mol^{-1} decreased with $T_{1/2}$ values of 150 and 352 K (Figure S4) to a plateau value of 25 cm^3 K mol^{-1} at 52 K. This indicates that desolvation of the material results in more residual HS Fe(II) centers remaining at low temperatures. This may explain the discrepancy between single crystal and magnetic susceptibility measurements, as the samples were prone to desolvation (See Figure S2 of the ESI).

LIESST experiments were conducted for solvated samples of **1** to determine the photoexcitation response to red (800 nm) and green (532 nm) light. **1** displayed a photomagnetic response for both red and green light sources on irradiation at 5 K (Figure 4b). Upon heating of the sample following photoexcitation with the green laser, the $\chi_m T$ value continues to increase until 28.73 cm^3 K mol^{-1} at 57 K, after which it begins to fall off with a T_{LIESST} value of 77 K. Similarly, excitation under red light provoked a similar response, with a slightly larger increase in the $\chi_m T$ value to 29.67 cm^3 K mol^{-1} at 47 K with the same T_{LIESST} value of 77 K. For both photoexcited samples, the behavior of the samples beyond the critical temperature are similar to each other, aligning well with the solvated 4 K min^{-1} heating curve.

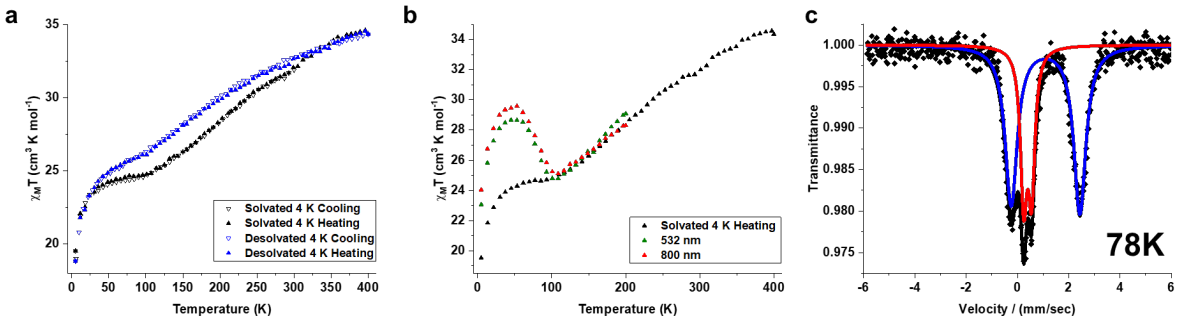

Figure 4. a) χ_mT *versus T* plot for solvated and desolvated **1** at scan rates of 4 K min^{-1}. b) Plot of LIESST experiments for solvated **1** with reference to 4 K min^{-1} heating cycle. c) Mössbauer spectra of solvated **1** at 78 K. The Fe(II) HS shown in blue and LS shown in red.

The Mössbauer experiment at 78 K for the solvated **1** supports the existence of both HS and LS Fe(II) centers. Two quadrupole-split doublets are identified (Figure 4c), the first doublet is wide (quadrupole-splitting Q.S. = 2.67 mm s^{-1} and an isomer shift I.S. = 1.09 mm s^{-1}), whereas the second doublet is narrow (Q.S. = 0.31 mm s^{-1} and I.S. = 0.40 mm s^{-1}), which represents the HS and LS states respectively. The area ratios of the Mössbauer absorption intensities of the HS and LS species (68:32) are in agreement with the $\chi_m T$ value of the magnetic susceptibility data (section S4 of the ESI), suggesting that the incomplete spin transition arises from three of the eight Fe(II) metal centers changing from HS to LS.

Magnetostructural Correlations

In order to investigate possible causes of the onset of SCO with the addition of the Ni(II) species to the cage faces, replacing Pd(II), a variety of intra- and intermolecular structural parameters were compared between the metalloligand, the $[Fe_8Pd_6\mathbf{L}_8]^{28+}$ cage that did not undergo SCO, and its Ni(II) analogue **1** that was SCO active. Firstly, the intramolecular parameters will be described, followed by examination of intermolecular and packing effects. A variety of structural parameters are presented in Table 1, and these demonstrate the various structural conformations that the metalloligands must undergo when coordinating the secondary metal ion and forming these cage architectures as well as reconformations that occur with SCO. The HS state was found to be fully occupied in the 100 K structures of $[Fe\mathbf{L}]^{2+}$, $[Fe_8Pd_6\mathbf{L}_8]^{28+}$ and the 275 K structure of **1**. The HS Fe-$N_{imidazolimine}$ bond lengths for the three structures all showed very similar values between 2.17 and 2.20 Å. Analysis of the angular parameters Σ and Θ suggests that the Fe(II) coordination environment of the metalloligand must distort much more severely from a perfect octahedron in the $[Fe_8Pd_6\mathbf{L}_8]^{28+}$ structure, with Σ and Θ values of 131.3 and 374.1˚, compared to much smaller values of 105.0 and 280.4˚ for the metalloligand and 105.0 and 273.0˚ for **1**. In other words, the

Fe(II) coordination environment of the metalloligand must severely distort when forming $[Fe_8Pd_6\mathbf{L}_8]^{28+}$, while in **1**, the coordination environment remains similar to that of the metalloligand. This large distortion of the Fe(II) coordination center in the $[Fe_8Pd_6\mathbf{L}_8]^{28+}$ structure may cause a large degree of intramolecular strain throughout the cage, and play a role in this structure remaining HS at low temperatures by increasing energetic barriers to reorganization of the coordination sphere required for SCO. Furthermore, occupation of antibonding orbitals by electron density from the axial acetonitrile donors, as well as the π-acceptor ability, may reduce the Ni-$N_{pyridine}$ bond order and allow the flexibility required of the coordination environment upon SCO.

In order to identify the extent of the metalloligand conformational change required to assemble the face centered cubic architecture, two further intramolecular structural parameters were calculated. The metalloligand secondary bonding axes angles (Figure 5a and S3.1 in the ESI), attempts to analyze the spread between tripodal ligand arms. The metalloligand secondary bonding axis was defined by the distal pyridyl N donor and the C opposite it in the pyridyl ring. In a perfect face-centered cubic cage structure where a tripodal metalloligand occupies the corners and connects to other metalloligands through coordination to a secondary metal on the face, any angles between two adjacent facial centers connected by a shared metalloligand would be approximately 60˚. Misalignment between the ligand arm's direction of approach towards the Ni center and the Fe-Ni axis allow some variations from the ideal value of 60˚. Next, the torsion angles arising in the pseudo C_3 axis between the coordinating imine N and the secondary pyridyl N on the same ligand arm (Figure 5b, c and S3.2 in the ESI), accounts for degree of twist within the metalloligand units occupying the cage corners. The torsion was calculated using the four points including the coordinating N_{imine}, the secondary pyridyl N on the same ligand arm, the centroid taken from the

three distal pyridyl-N positions with the pseudo C_3 Fe center, as well as the Fe center itself, in the order N_{imine}-Fe(II)-Fe(centroid)-$N_{pyridine}$ (Figure 5b).

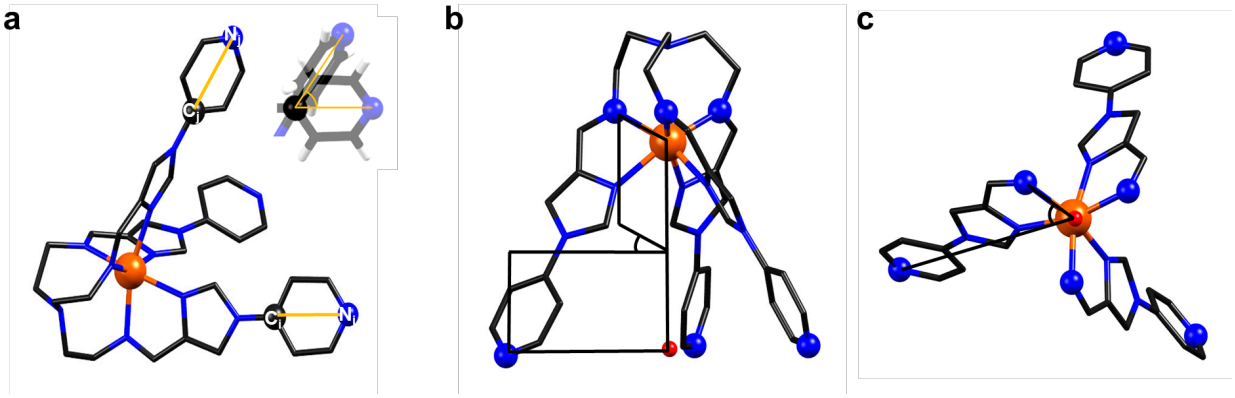

Figure 5. Schematics demonstrating the structural parameters used to quantify the degree of spread and twist experienced by the secondary donor groups. a) Secondary bond axes between pyridine groups. C atoms from each pair are superimposed, and the angle between bonding axes is measured directly. b) Planes defined by the two sets of coordinates used in the torsion angle [N_{imine}-Fe(II)] and [Fe-centroid-$N_{pyridine}$]. c) Torsion angle [N_{imine}-Fe(II)-Fe(centroid)-$N_{pyridine}$] as viewed along the pseudo-threefold axis, defined by the Fe-centroid (red) interval.

Table 2. Secondary bonding axes and ligand torsion angle for $[FeL]^{2+}$, $[Fe_8Pd_6L_8]^{28+}$ and **1**.[47]

Compound	Secondary Bonding Axes (˚)	Ligand Torsion Angle (˚)
$[FeL]^{2+}$ (100 K)	55.3	50.1
$[Fe_8Pd_6L_8]^{28+}$ (100 K)	61.3	55.4

1 (100 K)	64.0	63.2
1 (150 K)	64.2	63.0
1 (200 K)	62.8	60.1
1 (250 K)	60.8	55.3
1 (275 K)	61.1	55.4

The average secondary bonding axes angles obtained for the metalloligand structure was 55.3˚, compared to 61.3˚ for $[Fe_8Pd_6\mathbf{L}_8]^{28+}$ (100 K only) and 61.1˚ for **1** at 275 K. This demonstrates that the angles between ligand arms for both $[Fe_8Pd_6\mathbf{L}_8]^{28+}$ and **1** HS structures must spread apart to accommodate binding to the secondary metal ion, and must do so to an almost identical extent. On the other hand, at 100 K the bond axis values in **1** increase to an average angle of 64.0˚. As such, for the metalloligand units of **1** to exhibit the LS state, they require the ability to obtain a greater angular spread. The torsion angles in the metalloligand were calculated to have an average of 50.1˚. In contrast, upon formation of the $[Fe_8Pd_6\mathbf{L}_8]^{28+}$ cage and **1** at 275 K (the HS structure) this value increased to 55.4˚. This shows that in both HS cage structures the degree of metalloligand twist must increase by 10.6% when forming the face centered cubic architecture compared to that of the unbound metalloligand. However, once the spin state of the system changes to LS Fe(II), the degree of twist becomes substantially higher, and the average torsion angle measured for the structure of **1** at 100 K was 63.2 ˚. This represents a 13.9% increase compared to the HS structure of **1** at 275 K. It can be seen that in order to coordinate a secondary metal, the ligand arms of the metalloligands must move away from one another and undergo a large twist. To facilitate SCO within these structures, more drastic conformational movements within the ligand arms of the

metalloligand—in regard to both the degree of twist and spreading of the ligand—must be allowed (Figure 6).

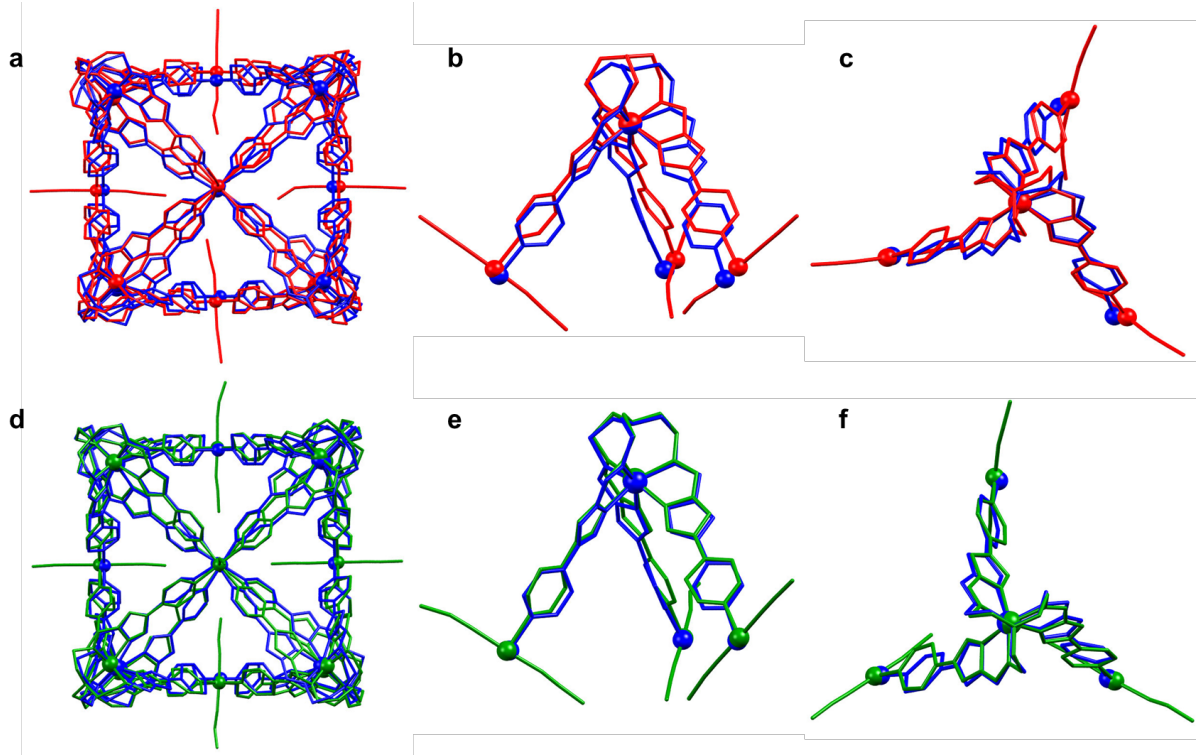

Figure 6. Overlay of crystal structures of HS $[Fe_8Pd_6\mathbf{L}_8]^{28+}$ (blue) at 100 K with LS **1** at 100 K (red) and HS **1** at 275 K (green). a) and d) View down the pseudo C_4 axis of $[Fe_8Pd_6\mathbf{L}_8]^{28+}$ and **1** respectively. b) and e) side view of metalloligand corners. c) and f) View down the pseudo C_3 axis of the metalloligand corners respectively.

Furthermore, inspection of the intramolecular distances between metal centers (Table 1) demonstrates the manner with which the cage shrinks and expands with SCO. The average Fe···Fe corner-to-opposite-corner distance (along the pseudo threefold symmetry axis of the cage) for the HS $[Fe_8Pd_6\mathbf{L}_8]^{28+}$ cage was 25.21 Å, in comparison to 25.58 Å for the HS structure of **1** at 275 K, indicating little difference. As the temperature was decreased to 100 K in **1**, this distance decreased from 25.58 to 24.86 Å in the LS structure. On the other hand, the average Ni···Ni distance from face-to-opposite-face along the pseudo fourfold symmetry axis for **1** in its HS configuration was

16.80 Å at 275 K, which again is similar to the analogous Pd···Pd distance of 16.30 Å. In the LS state of **1** (100 K), this distance increased to 17.26 Å. Therefore, the Fe···Fe and Ni···Ni distances are, firstly, longer in the HS Ni(II)-containing **1** than in the $[Fe_8Pd_6\mathbf{L}_8]^{28+}$ analogue, suggesting that the Pd(II) occupying the face contracts the structure inwards. Secondly, upon SCO the cage must contract along the Fe···Fe (corner-to-opposite-corner distance) threefold axis of the cage, while lastly, the Ni···Ni distance (face-to-opposite-face) must increase. This indicates that the structure must contract along the threefold axis and expand along the fourfold axis to facilitate SCO. Interestingly, as described above, the octahedral distortion parameters (Σ and Θ) of the Fe(II) centers increase drastically from the metalloligand in order to form $[Fe_8Pd_6\mathbf{L}_8]^{28+}$ (Table 1), while upon formation of **1** they remain very similar to those for the metalloligand. Furthermore, they must decrease dramatically to form the LS structure. Therefore, while the arms of the metalloigand must separate and twist further to reach the LS state, and the cage must contract down the threefold axis and expand outward along the fourfold axis, it may be the effect of the Pd(II) center on the octahedral environment of the Fe(II) centers, increasing both Σ and Θ dramatically, that causes significant intramolecular strain throughout the cage and prevents these necessary structural reorientations discussed above within the $[Fe_8Pd_6\mathbf{L}_8]^{28+}$ cage.

Another possible contributing factor for the onset of SCO in **1**, upon the introduction of Ni(II) to the cubic face, may be intermolecular in nature. A stark difference in the structures of **1** and the $[Fe_8Pd_6\mathbf{L}_8]^{28+}$ cage is the manner in which the cages pack in three dimensions. As can be seen in Figure 7a), both *Λ Λ Λ Λ Λ Λ Λ Λ* or *Δ Δ Δ Δ Δ Δ Δ Δ* homochiral enantiomers in $[Fe_8Pd_6\mathbf{L}_8]^{28+}$ pack in a very close nature, with the cages arranged face-to-face across mirror planes. The Pd(II) centers are positioned opposite one another on adjacent cages, separated by 6.9 Å, and the BF_4^- counter ions occupy this space between faces of the cages, providing very little free spacing.

Similarly the Fe(II) corners are directly adjacent and are separated by 8.6 Å. The solvent accessible volume calculated with a probe radius of 2 Å was 0.9% of the unit cell volume (Figure 7). On the other hand, the inclusion of $CH_3CN\cdots Ni$ bonding in the axial positions causes an offset packing arrangement (Figure 7b), where the corners of the cage pack closest to one another, nestling into the adjacent corner. The closest Fe(II) centers from adjacent cages are separated by 8.9 Å and the axial CH_3CN donors on the Ni(II) faces are directed towards the window of the offset adjacent cages with no appreciable intermolecular interactions. The nearest intermolecular Ni(II) centers are separated by 12.6 Å. The offsetting of cage packing in such a manner also produced much larger solvent accessible void spaces of 16.3% of the unit cell volume (Figure 7c). These voids are arranged throughout the spacing between the Ni(II) cage faces that results from the offset arrangement of contacting Fe(II) corners (Figure 7d). This demonstrates the conformational freedom provided to the Ni(II) faces by this packing arrangement. The closer packing of cage units is further illustrated by the crystal packing coefficient (the total percentage volume of the lattice occupied by the cage structure - see Table 1 and the ESI for full details), where $[Fe_8Pd_6\mathbf{L}_8]^{28+}$ at 100 K displayed a value of 33.4%, meanwhile for **1** the packing coefficient decreased to 28.7 and 27.0% for **1** at 100 and 275 K respectively. This represents a decrease in the total volume of the lattice occupied by the cage molecules of -4.7% in the HS structure of **1** as compared to $[Fe_8Pd_6\mathbf{L}_8]^{28+}$, demonstrating the relative extra conformational freedom provided by the packing arrangement of **1**. As demonstrated above, a variety of intramolecular arrangements must occur with SCO, these include the expansion of the angle between tripodal metalloligand arms, twisting within these arms, opposite Fe(II) corners must pull in towards one another and opposite M(II) faces must expand away from one another. In this way the offset packing arrangement of cages in

1 may provide a smaller barrier towards these necessary molecular rearrangements, more effectively permitting SCO throughout the material.

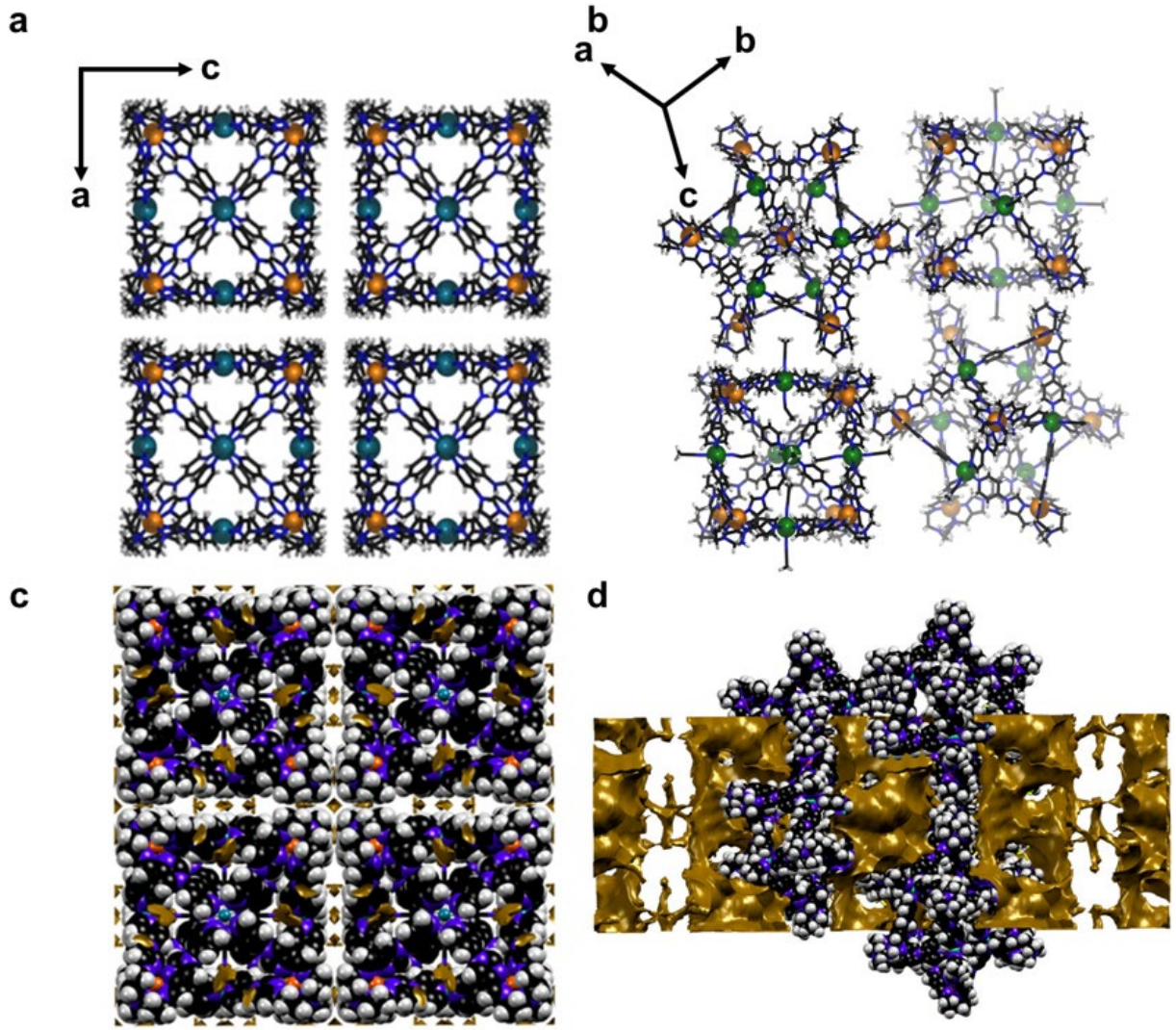

Figure 7. Schematic representation of single crystal packing of a) $[Fe_8Pd_6\mathbf{L}_8]^{28+}$ shown down the *b*-axis, b) Crystal packing of **1** viewed across the *b*-*c* plane, while c) and d) show space-filling representations of $[Fe_8Pd_6\mathbf{L}_8]^{28+}$ and **1** respectively (with atom sizes set to 0.5 times the Van der Waals radius) shown with calculated solvent accessible void spaces (gold) for a probe of 2 Å radius. Both c) and d) show four cage units, and d) further shows empty (white) spaces to either

side of the cages where four more cage units would occupy. The BF_4^- anions and solvent molecules were excluded (Fe, orange; Pd, navy blue; Ni, green; C, black; N, dark blue; H, white).

Conclusion

In this report, we present a new $[Fe_8Ni_6\mathbf{L}_8(CH_3CN)_{12}]^{28+}$ heterobimetallic cage **1** exhibiting SCO. In contrast, the previously reported $[Fe_8Pd_6\mathbf{L}_8]^{28+}$ analogue, differing by the identity of the linker metal species occupying the faces of the cage, remained HS at 100 K. Magnetic susceptibility measurements demonstrated that **1** exhibits gradual, two-step, incomplete spin transition, whereby three of the eight Fe(II) metal centers undergo SCO. Mössbauer experiments at 78 K displayed an area ratio of the Mössbauer absorption intensities for HS and LS species of approximately 68:32, supporting the magnetic susceptibility results. A notable LIESST effect was observed in **1** for both green and red light, corresponding to the excitation of approximately two Fe(II) centers. In contrast the VT-SCXRD experiment identified that **1** undergoes complete spin transition whereby the metalloligand corners of the cage exhibit a change in average Fe-N bond length from 1.97 to 2.17 Å. From a combination of magnetic susceptibility and VT-SCXRD experiments, it was proposed that a combined effect of inter- and intramolecular mechanisms may allow the $[Fe_8Ni_6\mathbf{L}_8(CH_3CN)_{12}]^{28+}$ structure to undergo SCO. The distorted octahedral coordination environment of the Ni(II) center may permit the requisite reconformation of the semi-rigid metalloigands for SCO, relative to the square planar Pd(II) coordination sphere. Furthermore, the presence of axially coordinated acetonitriles force the $[Fe_8Ni_6\mathbf{L}_8(CH_3CN)_{12}]^{28+}$ cages to pack in a more offset manner compared to the close packing of the Pd(II) structure, providing further conformational freedom. This was evidenced by the packing coefficient moving from 33.4 to 28.7% in the Pd and Ni structures respectively with a difference in solvent accessible voids from 0.3 to 16.9%. These results highlight the crucial role of the identity of the secondary metal and its

axial donors, in this case occupying the faces of the cubic cage, on the overall ability of the architecture to undergo intramolecular rearrangements that give rise to SCO. Clearly, as in the present study, a focus on the effect of secondary metal centers on the conformational properties of the metalloligand units as well as on the influence of axial donors on the packing arrangements of the resulting cage may both serve to inform the future design of multifunctional heteronuclear coordination cages possessing SCO capabilities.

Materials and Methods

Physical Measurements

Thermogravimetric analysis and differential scanning calorimetry (TGA-DSC) experiment was carried out on a NETZSCH STA-449 Jupiter Instrument. TGA-DSC measurements were acquired under a nitrogen atmosphere with a flow rate of 25 mL min^{-1} for both the purge and protective gases; sample was weighed into an aluminum crucible with a pierced lid and measurements were collected in a temperature range of 303 to 863 K at a rate of 10 K min^{-1}.

Scanning electron microscopy (SEM) and Energy dispersive spectroscopy (EDS) spot analysis and X-ray mapping were acquired using a Phenom XL in low vacuum with a chamber pressure of 10 Pa and accelerating voltage of 15 kV. All samples were mounted to an aluminum stub with double-sided conductive carbon tape and silicon wafers, images were taken uncoated. Spot EDS and X-ray mapping analysis was carried out using Phenom EDS software with a silicon drift detector (SDD).

Susceptibility data were collected using a Quantum Design SQUID magnetometer calibrated against a standard palladium sample. Single crystals were filtered from diffusion vials before air drying. Magnetic susceptibility measurements were collected between 5 K to 400 K at scan rates

of 1 and 4 K min^{-1} in cooling and heating modes. The sample was held at 400 K for 60 minutes to allow desolvation to take place, cooling and heating runs were collected for the desolvated sample from 400 K to 5 K to 400 K at scan rates of 1 and 4 K min^{-1}. Measurements were taken continuously under an applied field of 0.5 T.

Mössbauer experiments were conducted on a Wissel MVT-1000 Mössbauer spectrometer with a ^{57}Co/Rh source in a constant-acceleration transmission spectrometer (Topologic Systems) equipped with a closed-cycle helium refrigerator cryostat (Iwatani Co., Ltd.). All isomer shifts are given relative to α-Fe at room temperature.

Synthesis of cage 1. Nickel(II) tetrafluoroborate hexahydrate (107 mg, 0.31 mol) in 20 mL of CH_3CN was added dropwise to a solution of $[Fe\mathbf{L}]^{2+}$ (353 mg, 0.42 mol) in 10 mL of CH_3CN . The reaction mixture was heated to reflux with stirring for 1 h under a nitrogen atmosphere. The resulting orange solution was slowly diffused into di-isopropyl ether which resulted in the formation of dark red/orange crystals. The crystals were then isolated by filtration and air dried to give dark red/orange crystals of **1.** Yield: 259 mg, 57.0%. Elemental analysis (%) calculated, measured for **1**·59 H_2O: C (34.52, 34.64), H (4.86, 4.83), N (15.86, 15.73); Due to the quick decay of crystal after losing solvent (see Figure S2), powder X-ray diffraction experiments could not be conducted as the degradation of the crystals resulted in amorphous material.

Single crystal X-ray diffraction measurements.

Single crystal data for **1** were collected from the MX1 beamline at the Australian Synchrotron, using silicon double crystal chromated radiation (λ = 0.71073 Å) at 100, 150, 200, 250 and 275 K.[58] The single crystal data at 300 K could not be collected as the crystallinity started to wane off beyond 275 K, resulting in loss of diffraction. At the Australian synchrotron beamline, the XDS

software[59] was used for data integration, processing and scaling. The empirical absorption correction was then applied at the synchrotron using SADABS.[60] The structure was solved by ShelXT[61] using a suite of SHELX programs[62-63] via the Olex2 interface[64]. Non-hydrogen atoms were refined anisotropically for heterometallic cage **1** and hydrogen atoms were included in idealized position and refined using a riding model. The crystallographic data in CIF format has been deposited at the Cambridge Crystallographic Data Centre with CCDC number 2194121-2194125. The CIF is available free of charge from the Cambridge Crystallographic Data Centre, 12 Union Road, Cambridge CB2 1 EZ, UK; fax: (+44) 1223-336-033; or email: deposit@ccdc.cam.ac.uk. Crystals of heterometallic cage **1** diffracted only to lower angles of theta and therefore the data for **1** was collected at low resolution (~1.06Å). Structure of **1** at 100 and 150 K there are a total of five BF_4^- anions seen outside the cage with four BF_4^- anions present in the 200 K structure. Despite numerous attempts at modeling anions and solvents in the crystal lattice at 250 and 275 K, together with the low resolution (1.06 Å) and the thermal motion and disorder, the electron density of solvents and anions associated with them could not be found in the crystal lattice.

The non-hydrogen atoms of **1** at all temperatures were refined anisotropically with hydrogen atoms included in idealized positions and refined using a riding model. For all temperatures of **1**, the obtained geometry from the metalloligand was used to refine the atoms of the ligand. Restraints like RIGU and DFIX were used in the pyridyl, imidazole, Tren (tris(2-aminoethyl)amine) groups and the coordinating CH_3CN of the cage, and SADI ,RIGU and DFIX were used for the BF_4^- anions at lower temperatures. A solvent mask was applied to all temperatures for **1**, which found residual electron densities of 2820, 2870, 2876, 2696 and 2532 at 100, 150, 200, 250 and 275 K

respectively. The final R factors are in the range of (~0.12-0.14) with wR2 and GooF values in acceptable ranges for this large asymmetric unit in the monoclinic space group.

ASSOCIATED CONTENT

Physical measurements, crystallographic tables of complex, calculation of crystallographic parameters and magnetic susceptibility data, including Figures S1-S4 and Table S1 (PDF)

The Supporting Information is available free of charge on the ACS Publications website at DOI:_____. CCDC 2194121 - 2194125 contain the supplementary crystallographic data for this paper.

X-ray crystallographic data for **1** at 100 K (CIF)

X-ray crystallographic data for **1** at 150 K (CIF)

X-ray crystallographic data for **1** at 200 K (CIF)

X-ray crystallographic data for **1** at 250 K (CIF)

X-ray crystallographic data for **1** at 275 K (CIF)

AUTHOR INFORMATION

Corresponding Author

Feng Li - *School of Science, Western Sydney University, Locked Bag 1797, Penrith NSW 2751, Australia*; Email: feng.li@westernsydney.edu.au

Authors

Hyunsung Min - *School of Science, Western Sydney University, Locked Bag 1797, Penrith NSW 2751, Australia*

Alexander R. Craze - *School of Science, Western Sydney University, Locked Bag 1797, Penrith NSW 2751, Australia*

Matthew J. Wallis - *School of Science, Western Sydney University, Locked Bag 1797, Penrith NSW 2751, Australia*

Ryuya Tokunaga - *Department of Chemistry, Graduate School of Science and Technology, Kumamoto University, 2-39-1 Kurokami, Chuo-ku, Kumamoto 860-8555, Japan*

Takahiro Taira - *Department of Chemistry, Graduate School of Science and Technology, Kumamoto University, 2-39-1 Kurokami, Chuo-ku, Kumamoto 860-8555, Japan*

Yutaka Hirai - *Department of Chemistry, Graduate School of Science and Technology, Kumamoto University, 2-39-1 Kurokami, Chuo-ku, Kumamoto 860-8555, Japan*

Mohan M. Bhadbhade - *Mark Wainwright Analytical Centre, University of New South Wales, Kensington, NSW, 2052, Australia*

Daniel J. Fanna - *Advanced materials Characterisation Facility, Western Sydney University, Locked Bag 1797, Penrith NSW 2751, Australia*

Christopher E. Marjo - *Mark Wainwright Analytical Centre, University of New South Wales, Kensington, NSW, 2052, Australia*

Shinya Hayami - *Department of Chemistry, Graduate School of Science and Technology, Kumamoto University, 2-39-1 Kurokami, Chuo-ku, Kumamoto 860-8555, Japan*

Leonard F. Lindoy - *School of Chemistry F11, The University of Sydney, NSW 2006, Australia*

Present Addresses

Alexander R. Craze - *Department of Chemistry, University of Oxford, 12 Mansfield Road, Oxford OX1 3TA, UK*

Notes

The authors declare no competing conflict of interest.

ACKNOWLEDGMENT

The authors would like to thank Western Sydney University (WSU) for research funding, the Advanced Materials Characterisation Facility (AMCF) at WSU, Mark Wainwright Analytical Centre at UNSW and Kumamoto University at which the magnetic susceptibility, Mössbauer and CHN experiments were conducted. The crystallographic experiments were performed on the MX1 beamline of the Australian Synchrotron, Clayton, Victoria, Australia. We also thank the Australian Synchrotron for the travel support and their staff for beamline assistance.

References

1 McConnell, A. J. *Chem. Soc. Rev.* **2022**, *51*, 2957-2971.

2 McTernan, C. T.; Davies, J. A.; Nitschke, J. R. *Chem. Rev.* **2022**, *122*, 10393-10437.

3 Ning X.; Tan Y-X.; El-Sayed, E.-S. M. *Cryst. Growth Des.* **2022**, *22*, 2768-2773.

4 Li, W.; Li, S.; Liu, C.; Rotaru, A.; Robeyns, K.; Singleton, M. L.; Garcia, Y. *J. Mater. Chem. C.* **2022**, *10,* 9216-9221.

5 Li, Y-W.; Li, J.; Wan, X-Y.; Shen, D-F.; Yan, H.; Zhang, S-S.; Ma, H-Y.; Wang, S-N.; Li, D-C.; Gao, Z-Y.; Dou, J-M.; Sun, Di. *Inorg. Chem.* **2021**, *60*, 671-681.

6 Zhang, Z.; Zhao, Z.; Wu, L.; Lu, S.; Ling, S.; Li, G.; Xu, L.; Ma, L.; Hou, Y.; Wang, X.; Li, X.; He, G.; Wang, K.; Zou, B.; Zhang, M. *J. Am. Chem. Soc.* **2020**, *142*, 2592-2600.

7 Lu, Y-L.; Song, J-Q.; Qin, Y-H.; Guo, J.; Huang, Y-H.; Zhang, X-D.; Pan, M.; Su, C-Y. *J. Am. Chem. Soc.* **2022**, *144*, 8778-8788.

8 Xue, Y.; Hang, X.; Ding, J.; Li, B.; Zhu, R.; Pang, H.; Xu, Q. *Coord. Chem. Rev.* **2021**, *430*, 213656.

Tan, C.; Chu, D.; Tang, X.; Liu, Y.; Xuan, W.; Cui, Y. *Chem. Eur. J.* **2019**, *25*, 662-672.

10 Gao, W-X.; Zhang, H-N.; Jin, G-X. *Coord. Chem. Rev.* **2019**, *386*, 69-84.

11 Preston, D.; Lewis, J. E. M.; Crowley, J. D. *J. Am. Chem. Soc.* **2017**, *139*, 2379-2386.

12 Zhen, Y-R.; Suntharalingam, K.; Johnstone, T. C.; Lippard, S. J. *Chem. Sci.* **2015**, *6*, 1189-1193.

13 Zhu, C.; Yang, K.; Wang, H.; Fang, Y.; Feng, L.; Zhang, J.; Xiao, Z.; Wu, X.; Li, Y.; Fu, Y.; Zhang, W.; Wang, K-Y.; Zhou, H-C. *ACS Cent. Sci.* **2022**, *8*, 562-570.

14 Zhang, D.; Ronson, T. K.; Zou, Y-Q.; Nitschke, J. R. *Nat. Rev. Chem.* **2021**, *5*, 168-182.

15 Jackson, G. D.; Tipping, M. B.; Taylor, C. G. P.; Piper, J. R.; Pritchard, C.; Mozaceanu, C.; Ward. M. D. *Chemistry*, **2021**, *3*, 1203-1214.

16 Yadav, S.; Kannan, P.; Qiu, G. *Org. Chem. Front.* **2020**, *7*, 2842-2872.

17 Brzechwa-Chodzyńska, A.; Drożdż, W.; Harrowfield, J.; Stefankiewicz, A. R. *Coord. Chem. Rev.* **2021**, *434*, 213820.

18 Hu, X.; Han, M.; Shao, L.; Zhang, C.; Zhang, L.; Kelley, S. P.; Zhang, C.; Lin, J.; Dalgarno, S. J.; Atwood, D. A.; Feng S.; Atwood, J. L. *Angew. Chem. Int. Ed.* **2021**, *60*, 10516-10520.

19 Wezenber, S. J. *Chem. Lett.* **2020**, *49*, 609-615.

20 Hardy, M.; Lützen, A. *Chem. Eur. J.* **2020**, *26*, 13332-13346, 10.1002/chem.202001602.

21 McConnell, A. J. *Supramolecular Chemistry*, **2018**, *30*, 858-868.

22 Glatz, J.; Chamoreau, L-M.; Flambard, A.; Meunier, J-F.; Bousseksou, A.; Lescouëzec, R. *Chem. Commun.* **2020**, 56, 10950-10953.

23 Hardy, M.; Tessarolo, J.; Holstein, J. J.; Struch, N.; Wagner, N.; Weisbarth, R.; Engeser, M.; Beck, J.; Horiuchi, S.; Clever, G. H.; Lützen, A. *Angew. Chem. Int. Ed.* **2021**, *60*, 22562-22569.

24 Berdiell, I. C.; Hochdörffer, T.; Desplanches, C.; Kulmaczewski, R.; Shahid, N.; Wolny, J. A.; Warriner, S. L.; Cespedes, O.; Schünemann, Chastanet, G.; Halcrow, M. A. *J. Am. Chem. Soc.* **2019**, *141,* 18759-18770.

25 Zhang, F-L.; Chen, J-Q.; Qin, L-F.; Tian, L.; Li, Z.; Ren, X.; Gu, Z-G. *Chem. Commun.* **2016**, *52*, 4796-4799.

26 Li, L.; Saigo, N.; Zhang, Y.; Fanna, D. J.; Shepherd, N. D.; Clegg, J. K.; Zheng, R.; Hayami, S.; Lindoy, L. F.; Aldrich-Wright, J. R.; Li, C-G.; Reynolds, J. K.; Harman, D. G.; Li, F. *J. Mater. Chem. C.* **2015**, *3*, 7878-7882.

27 Li, L.; Craze, A. R.; Mustonen, O.; Zenno, H.; Whittaker, J. J.; Hayami, S.; Lindoy, L. F.; Marjo, C. E.; Clegg, J. K.; Aldrich-Wright, J. R.; Li, F. *Dalton Trans.* **2019**, *48*, 9935-9938.

28 Howard-Smith, k. J.; Craze, A. R.; Zenno, G.; Yagyu, J.; Hayami, S.; Li, F. *Chem. Commun.* **2020**, *56*, 8838-8841.

29 Craze, A. R.; Bhadbhade, M. M.; Komatsumaru, Y.; Marjo, C. E.; Hayami, S.; Li, F. *Inorg. Chem.* **2020**, *59*, 1274-1283.

30 Craze, A. R.; Sciortino, N. F.; Bhadbhade, M. M.; Kepert, C. J.; Marjo, C. E.; Li, F. *Inorganics*, **2017**, *5*, 62.

31 Craze, A. R.; Bhadbhade, M. M.; Kepert, C. J.; Lindoy, L. F.; Marjo, C. E.; Li, F. *Crystals*, **2018**, *8,* 376.

32 Li, L.; Neville, S. M.; Craze, A. R.; Clegg, J. k.; Sciortino, N. F.; Athukorala Arachchige, K. S.; Mustonen, O.; Marjo, C. E..; McRae, C. R.; Kepert, C. J.; Lindoy, L. F.; Aldrich-Wright, J. R.; Li, F. *ACS Omega.* **2017**, *2*, 3349-3353.

33 Craze, A. R.; Howard-S,ith, K. J.; Bhadbhade, M. M.; Mustonen, O.; Kepert, C. J.; Marjo, C . E.; Li, F. *Inorg. Chem.* **2018**, *57*, 6503-6510.

34 Hogue, R. W.; Singh, S.; Brooker, S. *Chem. Soc. Rev.* **2018**, *47*, 7303-7338.

35 Ren, D-H.; Qiu, D.; Pang, C-Y.; Li, Z.; Gu, Z-G. *Chem. Commun.* **2015**, *51*, 788-791.

36 Ferguson, A.; Squire, M. A.; Siretanu, D.; Mitcov, D.; Mathonière, C.; Clérac, R.; Kruger, P. E. *Chem. Comm.* **2013**, *49,* 1597-1599.

37 Bilbeisi, R. A.; Zarra, S.; Feltham, H. L. C.; Jameson, G. N. L.; Clegg, J. K.; Brooker, S.; Nitschke, J. R. *Chem. Eur. J.* **2013**, *19*, 8058-8062.

38 Struch, N.; Bannwarth, C.; Ronson, T. K.; Lorenz, Y.; Mienert, B.; Wagner, N.; Engeser, M.; Bill, E.; Puttreddy, R.; Rissanen, K.; Beck, J.; Grimme, S.; Nitschke, J. R.; Lützen, A. *Angew. Chem. Int. Ed.* **2017**, *56*, 4930-4935.

39 Duriska, M. B.; Neville, S. M.; Moubaraki, B.; Cashion, J. D.; halder, G. J.; Chapman, K. W.; Balde, C.; Létard, J-F.; Murray, K. S.; Kepert, C. J.; Batten, S. R. *Angew. Chem.* **2009**, *121*, 2587-2590.

40 Duriska, M. B.; Neville, S. M.; Moubaraki,; Murray, K. S.; Balde, C.; Létard, J-F.; Kepert, C. J.; Batten, S. R. *ChemPlusChem.* **2012**, *77*, 616-623.

41 Lu, H-S.; Han, W-K.; Yan, X.; Xu, Y-X.; Zhang, H-X.; Li, T.; Gong, Y.; Hu, Q-T.; Gu, Z-G. *Dalton Trans.* **2020**, *49*, 4420-4224.

42 Berdiell, I. C.; Hochdörffer.; Desplanches, C.; Kulmaczewski, R.; Shahid, N.; Wolny, J. A.; Warriner, S. L.; Cespedes, O.; Schünemann, V.; Chastanet, G.; Halcrow, M. A. *J. Am. Chem. Soc.* **2019**, *141*, 18759-18770.

43 Zhang, D.; Ronson, T. K.; Nitschke, J. R. *Acc. Chem. Res.* **2018**, *51*, 2423-2436.

44 Cook. T. R.; Stang, p. J. *Chem. Rev.* **2015**, *115*, 7001-7045.

45 Fujita, m.; Umemoto, K.; Yoshizawa, M.; Fujita, N.; Kusukawa,T.; Biradha, K. *Chem. Commun.* **2001**, 509-518.

46 Zhou, X-C.; Wu, L-X.; Wang, X-Z.; Lai, Y-L.; Ge, Y-Y.; Su, J.; Zhou, X-P.; Li D. *Inorg. Chem.* **2022**, *61*, 5196-5200.

47 Min, H.; Craze, A.; Tairo, T.; Wallis, M. J.; Bhadbhade, M. M.; Tian, R.; Fanna, D. J.; Wuhrer, R.; Hayami, S.; Clegg, J. K.; Marjo, C. E.; Lindoy, L. F.; Li, F. *Chemistry*, **2022**, *4*, 535.

48 Sudan, S.; Li, R-J.; Jansze, S. M.; Platzek, A.; Rudolf, R.; Clever, G. H.; Fadaei-Tirani, F.; Scopelliti, R.; Severin, K. *J. Am. Chem. Soc.* **2021**, *143*, 1773-1778.

49 Hardy, M.; Struch, N.; Topić, F.; Schnakenburg, G.; Rissanen, K.; Lützen, A. *Inorg. Chem.* **2018**, *57*, 3507-3515.

50 Zhang, Y-Y.; Gao, W-X.l Lin, L.; Jin, G-X. *Coord. Chem. Rev.* **2017**, *344*, 323-344.

51 Li, L.; Fanna, D. J.; Shepherd, N. D.; Lindoy, L. F.; Li, F. *J. Incl. Phenom. Macrocycl. Chem.* **2015**, *82*, 3-12.

52 Li, L.; Zhang, Y.; Avdeev, M.; Lindoy, L. F., Harman D. G.; Zhen, R.; Cheng, Z.; Aldrich-Wright, J. R.; Li, F. *Dalton Trans*. **2016**, *45*, 9407-9411.

53 Li, F.; Lindoy, L. F. *Aust. J. Chem.* **2019**, *72*, 731.

54 Reichel, F.; Clegg, J. K.; Gloe, K.; Gloe, K.; Weigand, J. J.; Reynolds, J. K.; Li, C-G.; Aldrich-Wright, J. R.; Kepert, C. J.; Lindoy, L. F.; Yao, H-C.; Li, F. *Inorg. Chem.* **2014**, *53*, 688-690.

55 Pullen, S.; Tessarolo, J.; Clever, G. H. *Chem. Sci.* **2021**, *12*, 7269-7293.

56 Ketkaew, R.; Tantirungrotechai, Y.; Harding, D.J.; Harding, P.; Chastanet, G.; Guionneau, P.; Marchivie, M. *Dalton Trans.* **2021**, *50*, 1086-1096.

57 Schmitz, S.; Leusen, J. V.; Ellern, A.; Kögerler, P.; Monakhov, K. Y. *Inorg. Chem. Front.* **2016**, *3*, 523-531.

58 Cowieson, N.P.; Aragao, D.; Clift, M.; Ericsson, D.J.; Gee, C.; Harrop, S.J.; Mudie, N.; Panjikar, S.; Price, J.R.; Riboldi-Tunnicliffe, A.; et al. *J. Synchrotron Rad.* **2015**, *22*, 187–190.

59 Kabsch, W. XDS. *J. Appl. Crystallogr.* **1993**, *26*, 795–800.

60 SADABS, version 2014/5; Bruker AXS Inc.: Madison, WI, USA, **2001**.

61 Sheldrick, G.M. *Acta. Cryst*. A **2015**, *71*, 3–8.

62 Sheldrick, G.M. SHELX-2014: Programs for Crystal Structure Analysis; University of Göttingen: Göttingen, Lower Saxony, Germany, **2014**.

63 Sheldrick, G.M. *Acta. Cryst. C.* **2015**, *71*, 3–8.

64 Dolomanov, O.V.; Bourhis, L.J.; Gildea, R.J.; Howard, J.A.K.; Puschmann, H. *J. Appl. Cryst.* **2009**, *42*, 339–341.